Numerical Investigation of Turbulent Flow around a Recent Horizontal Axis Wind Turbine using Low and High Reynolds Models

A. Bouhelal[1,3†], A. Smaili[1], O. Guerri[2] and C. Masson[3]

[1] *Mechanical Engineering and Development Laboratory, École Nationale Polytechnique, B.P. 182, El-Harrach, Alger, 16200, Algeria*
[2] *Centre de Développement des Énergies Renouvelables, B.P. 62, Route de l'Observatoire, Bouzaréah, Alger, Algeria*
[3] *Department of Mechanical Engineering, École de Technologie Supérieure, 1100 Notre-Dame Ouest, H3C1K3, Montréal, Québec, Canada*

†*Corresponding author email: abdelhamid.bouhelal@g.enp.edu.dz*

ABSTRACT

The effects of different Reynolds Averaged Navier Stokes (RANS) turbulence models on two near-wall approaches using high and low Reynolds models on predicting performance of horizontal axis wind turbines (HAWTs) were studied for a range of wind conditions where flow over the rotor varied from fully attached to massively separated flow. This paper's main contribution is in establishing which RANS models can produce quantitatively reliable numerical predictions of turbulent flow around wind turbine rotors. The authors used measurements done by the new MEXICO (Model rotor EXperiments In COntrolled conditions) project in the German Dutch wind tunnels (DNW) in order to validate and test CFD (Computational Fluid Dynamic) codes. Four different RANS turbulence models were considered: Spalart-Allmaras; $k - \varepsilon$ (RNG); $k - \omega$ SST; and the transition γ-Re_θ model. At low wind speeds, it was found that all four models were good predictors of aerodynamic performance, and at high wind speeds, where the swirl effect was modeled using wall function corrections in both equations, the $k - \varepsilon$ model was considered to be the best model: it was the most accurate within a reasonable computational time.

Keywords: Aerodynamic analysis; HAWT; CFD; Turbulence modeling; RANS; low and high Reynolds Models; Near-wall treatment; New MEXICO measurement.

NOMENCLATURE

C_p	pressure coefficient	x_i	position vector
e_a	relative error	$y+$	dimensionless wall distance
F_n	normal force	γ	intermittency
F_t	tangential force		
GCI	Grid Convergence Index	$\overset{=}{\tau}$	shear stress tensor
h	mesh size		
I	unit tensor	$\vec{\omega}$	angular velocity
k	turbulence kinetic energy	ξ	apparent order
N	total number of cells	$\vec{u}$	fluid velocity
P	static pressure		
r	refinement factor	$\tau_{ij} = \rho \overline{u_i' u_j'}$	Reynolds stress tensor
Re_θ	thickness Reynolds number	μ	dynamic viscosity
u	exact velocity component	ΔV_i	cell volume
U	average velocity component	ε	dissipation rate of kinetic energy
u'	fluctuating velocity component	ρ	fluid density
u_i	inertial reference frame velocity	φ	variable key of GCI method
u_r	rotating reference frame velocity	ω	specific dissipation rate

1. INTRODUCTION

Along with increasing global energy needs and growing environmental concerns, the search for new, efficient and inexhaustible energy sources is an obligation, not a choice. Recently, the world has seen unprecedented progress in the field of renewable energy. According to the International Energy Agency's 2012 report ((IEA), 2012), the share of renewables in worldwide electricity generation is projected to reach 31% by 2035, a quarter of which will be from wind power alone.

Wind energy offers the possibility of exploiting the kinetic energy of wind, using it to produce electrical energy by means of rotating machines (wind turbines). Since interest in generating electricity using wind turbines began, several different types of machines have been developed. At present, the machine most commonly used for harvesting wind energy in the field of application is the horizontal axis wind turbine (HAWT) (Aranake, Lakshminarayan, and Duraisamy, 2015).

Due to the high cost of studying wind turbines experimentally, it was necessary for us to use and develop numerical methods that would allow us to predict wind energy and find ways to exploit it. In order to study wind turbine rotor aerodynamics, one needs to be able to model the rotor under both its operating conditions and its interactions with the wind, and this to a certain degree of accuracy. Several techniques exist: methods involving Computational Fluid Dynamics (CFD), vortex methods, and Blade Element Momentum (BEM). Each has its advantages (Guntur and Sørensen, 2013).

Aerodynamic methods using CFD with full rotor geometry are the most efficient and the most precise; however, such methods are quite complex due to the fact that these problems are described by the so-called Navier-Stokes equations, which cannot be solved analytically: the fact that analytical solutions of the Navier-Stokes equations "only" demonstrate the existence of smooth solutions is, in fact, one of the seven Millennium Prize Problems (Schepers *et al.*, 2012).

A numerical solution for the Navier-Stokes equations for all time and length scales (Direct Numerical Simulation) was also out of reach, due to the extreme demands it would make on computational resources. This remains true even on the most modern computer clusters. Schepers (Shepers, 2012) has shown that computational effort for wind energy applications is even more extreme than it is for most other applications (e.g. aerospace) due to blade rotation and the presence of turbulence.

The modeling of turbulence is seen as a key element in CFD applications. Up until now, unfortunately, no single model exists that allows us to predict all the classes of physical phenomena linked to turbulence.

Today there are many different turbulence models, and each model fits its own phenomenon and cannot serve for other phenomena. This is unsurprising, since the main objective of turbulence modeling is to attempt to approximate a highly complicated phenomenon (Wilcox, 1993).

The simplest turbulence models available in the literature are based on solving the Reynolds Averaged Navier-Stokes equations (RANS); these models are based on the resolution of the average flow field using additional transport equations to close the open system caused by additional unknowns in the equations produced by the Reynolds averaging process (ANSYS Fluent, 2016; Wilcox, 1993).

The acceptance, validation and development of CFD tools for wind turbines have all depended, in large part, on the availability of good experimental data under controlled conditions. The NREL/NASA AMES wind tunnel experiment in 1999 (Fingersh *et al.*, 2001; Simms, Schreck, Hand, and Fingersh, 2001) may be the most well known experiment of recent decades. The NREL experiments focused mainly on rotor aerodynamics and less on wake behaviour.

The experimental measurements conducted by NREL (Schreck, 2002) focused on aerodynamic loads on the rotor, disregarding wake behaviour; given the absence of detailed flow measurements using advanced techniques such as laser Doppler anemometry (LDA) and particle image velocimetry (PIV), this led the Energy Research Centre of the Netherlands (ECN) and its partners to perform highly successful aerodynamic experiments in Europe's largest wind tunnel, under a program called the MEXICO project (Model rotor EXperiments In COntrolled conditions) (Boorsma and Schepers, 2014; Snel,Schepers, and Montgomerie, 2007).

These MEXICO experiments were carried out in the large-scale, low-speed facility (LLF) at the German Dutch wind tunnels (DNW), a high-quality wind tunnel with a 9.5 x 9.5 m^2 open test section. The first series of experiments were performed in December 2006 (Schepers *et al.*, 2012; Snel, Schepers, and Siccama, 2009 ; Snel *et al.*, 2007). Between June 20 and July 4, 2014, the new MEXICO measurements followed up the first test campaign, using the same model (Boorsma and Schepers, 2014; Schepers *et al.*, 2014).

In addition to detailed rotor load measurements on the wind turbine blades and detailed PIV measurements in the wake contained in both the MEXICO and the new MEXICO measurements, another unique feature of the new MEXICO experiment was the availability of both natural and tripped flow conditions: these allowed for an investigation into the effect of laminar/turbulent transition (Sørensen, Zahle, Boorsma, and Schepers, 2016).

Another advantage of using the MEXICO model is the fact that these measurements were performed in the open test section of the wind tunnel at DNW, at very low turbulence intensity (Boorsma and Schepers, 2014); this rendered the effect of tunnel geometry negligible, as had already been demonstrated in a previous study (Shen, Zhu, and Sørensen, 2012). The results can thus be generalized

Fig.1. (a) The German Dutch wind tunnels (DNW), and (b) The MEXICO wind turbine model.

for cases under real atmospheric conditions and for full-scale wind turbine applications.

Several RANS turbulence models have been used in the literature and within the framework of the numerical simulation of turbulent flow around wind turbines. The models most frequently used have been based on two transport equations: for example, the $k - \omega$ SST turbulence model was used by (Moshfeghi, Song, and Xie, 2012; Plaza, Bardera, and Visiedo, 2015; Sorensen, Michelsen, and Schreck, 2002), and $k - \varepsilon$ models were used by (Bouhelal, Smaili, Masson, and Guerri, 2017; Elfarra, Sezer‑Uzol, and Akmandor, 2014; Thumthae and Chitsomboon, 2009).

Historically, there are two approaches to applying RANS turbulence models in cases of flow around wind turbine blades: either via full near-wall resolution (low Reynolds models) using a sufficient fine mesh in the near wall to capture the boundary layer and the point of separation, or via a wall function approach that avoids near-wall spatial resolution. This technique is called the high Reynolds model approach, and its main advantage is that it reduces calculation time by reducing computational mesh size (Abdulqadir, Iacovides, and Nasser, 2016; ANSYS Fluent, 2016).

The main goal of this study has been to evaluate the sensitivity of various RANS turbulence models' accuracy in the numerical prediction of HAWT aerodynamic performance, using detailed recent new MEXICO measurements. The investigation includes four radically different turbulence models in two near-wall approaches:

- High Reynolds models: (Spalart-Allmaras and $k - \varepsilon$ (RNG)).

- Low Reynolds models: ($k - \omega$ SST and transition γ-Re$_\theta$ model).

The simulation covered three cases in axial flow, where the flow changed from fully attached to massively separated. This allowed us to identify the strengths and weaknesses of the selected turbulence models along a wide range of flows. The ANSYS

Fluent 17.2 solver based on the finite volume method was used in all investigations.

2. DESCRIPTION OF WIND TURBINE MODEL

The new MEXICO experiments were performed from June 20 to July 4, 2014, in the large-scale, low-speed facility (LLF) at the German Dutch wind tunnels (DNW) (Fig.1 (a)): a high-quality atmospheric, closed-circuit wind tunnel with an open jet 9.5 x 9.5 m^2 section. The MEXICO rotor was placed between the nozzle and the collector at distances of 7 and 13 metres, respectively.

The MEXICO rotor (Fig.1 (b)) is a three-bladed model equipped with a pitch actuator and speed controller. An overview of a detailed MEXICO wind turbine within the framework of new MEXICO measurements is shown in Table 1.

Table 1 General MEXICO wind turbine information

Rotation direction	Clockwise
Power regulation	Not present, speed control by motor/generator
Number of blades	3
Rotational speed	425.5 (rpm)
Rotor diameter	4.5 (m)
Blade material	Aluminum 7075-T651 Alloy
Global pitch angle	-2.3 (°)
Tower height	5.12 (m)

The MEXICO blade is aerodynamically complicated, when compared with other blade models such as NREL blades; the MEXICO blade is composed of three different families of aerodynamic profiles (Boorsma and Schepers, 2014; Oggiano, Boorsma, Schepers, and Kloosterman, 2016):

- The DU91-W2-250, airfoil developed at Delft University of Technology, is applied to the root of the blade, from 20 to 45.6% span.

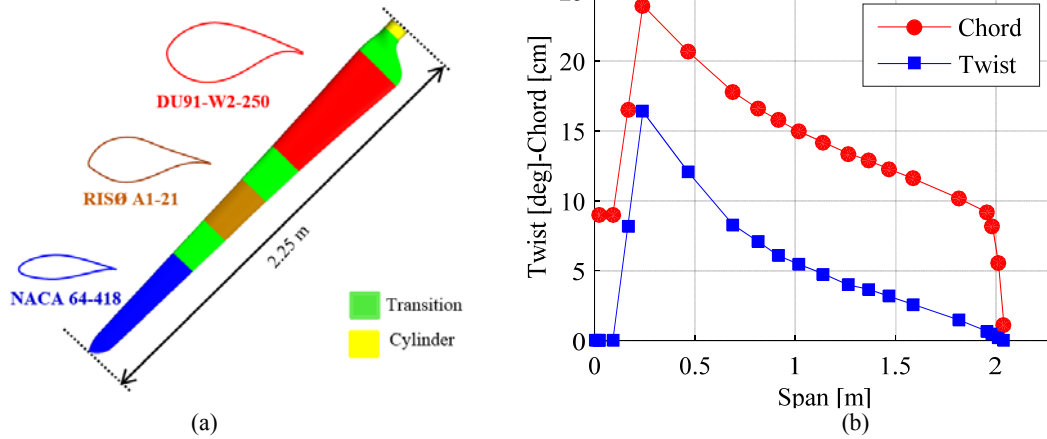- The RISØ-A1-21 airfoil, developed at the

Fig. 2. (a) Twist/chord distribution along the blade span, and (b) The MEXICO blade airfoil configuration.

National Laboratory of Denmark, is applied from 54.4% to 65.6% in mid span.

- The NACA 64-418 airfoil, designed by the National Advisory Committee for Aeronautics at NASA, is applied in the outer part from 74.4% span.

The distribution of twist and chord along the MEXICO blade span is shown in Fig. 1 (a). From this figure, we see that twist can reach (16.4°) as the maximum value in the root part of the blade. The blade's configuration is shown in Fig. 1 (b). For more information on tunnel geometry and turbine details, see (Boorsma and Schepers, 2014; Oggiano *et al.*, 2016; Schepers *et al.*, 2012; Schepers *et al.*, 2014; Snel *et al.*, 2009; Snel *et al.*, 2007).

3. NUMERICAL METHOD

In this project, steady simulations were carried out based on the numerical resolution of the Navier-Stokes equations using a finite-volume method based on a cell-centered scheme using the ANSYS Fluent 17.2 CFD solver. Since wind speeds around wind turbines are habitually quite low compared to sound speed, where the Mach number does not exceed 0.3, we may consider the flow as incompressible, and its properties as constants.

In this study, the simulations cover three no-yawed flow conditions, where flow over the MEXICO rotor varies from fully attached to massively separated. The operating flow conditions for the three cases investigated in this study are shown in Table 2.

Table 2 Operating conditions for the three cases using new MEXICO measurements

Case	U_{tunnel} (m/s)	ρ (Kg/m³)	P (Pa)
1	10.05	1.197	101398
2	15.06	1.191	101345
3	24.05	1.195	101407

3.1 Computational Domain

The 3D geometry of the MEXICO blade was generated based on three datasets of 2D airfoil coordinates: (DU91-W2-250, RISØ-A1-21 and NACA 64-418) as well as on the detailed blade geometry given in reference (Boorsma and Schepers, 2014) using SolidWorks Software (Fig. 3).
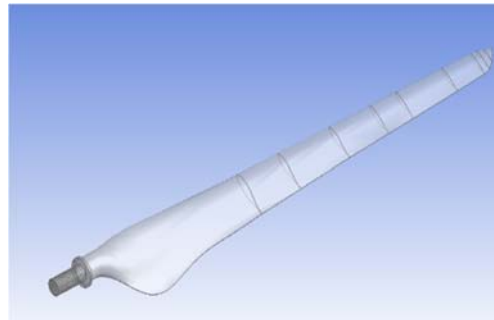

Fig. 3. Three-dimensional geometry of the MEXICO blade model.

It was not necessary to take the full geometry of a wind turbine (tower and nacelle) into account in CFD simulations under no-yawed flow conditions, according to (Sorensen *et al.*, 2002), and, in order to reduce computational time due to the symmetry flow field around the MEXICO rotor, the computational domain was constructed only on one blade, representing one-third of the full rotor geometry exploiting the 120° symmetry of the computational domain.

The inlet boundary of the computational domain was located five blade radii upstream, and the outlet was located ten blade radii downstream (Fig. 4). The radius of the computational domain was five blade radii. A small zone close to the blade with a diameter of two blade radii and a length of one blade radii was designed with two goals in mind: separating the rotating part into stationary parts, and refining the grid in the near-blade region.
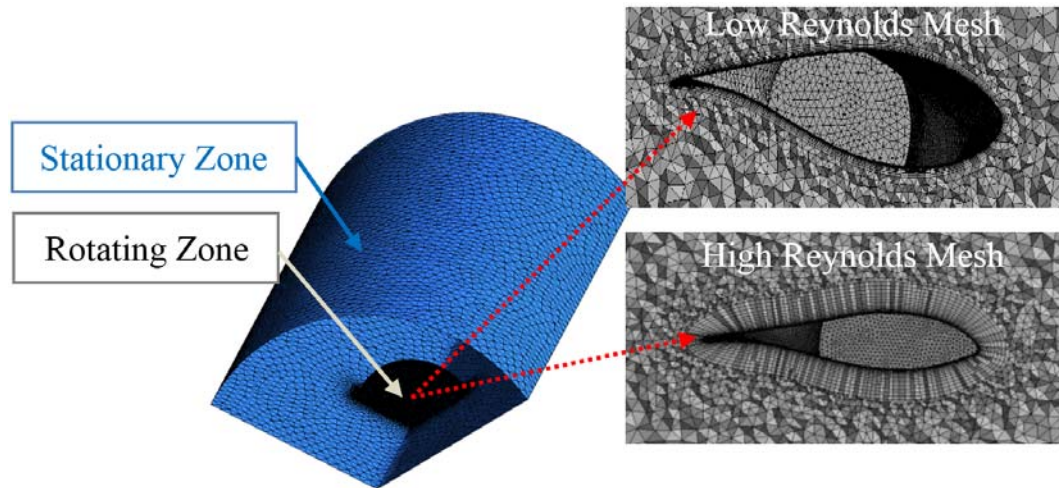
Fig. 4. Computational mesh for low and high Reynolds models.

3.2 Mathematical Model

In this study, simulation of the flow around the MEXICO blade was carried out using the numerical resolution of the averaged Navier-Stokes equations (RANS) in the Cartesian coordinates system closed by four different turbulence models. The computational domain was divided into two parts: the rotating part and the stationary part, as illustrated in Fig.4. The Multiple Reference Frame (MRF) was applied in the zone close to the blade (the rotating part). This will be discussed in Section 3.2.1. In the stationary part of the computational domain, the RANS equations modeled in the inertial frame were applied: these are discussed in Section 3.2.2.

3.2.1 Blade Rotation Modeling

The Multiple Reference Frame (MRF) model (Luo and Gosman, 1994) is the simplest model used for modeling flow field over rotating objects; this steady-state approach is based on the additional terms in the momentum equations, which lead to an increase in acceleration of fluid resulting from the blades' rotation (ANSYS Fluent, 2016). The transformation of fluid velocities from the stationary frame to the moving frame, using the notation *i* for *inertial* and *r* for *rotating* can be expressed as follows:

$$\vec{u}_r = \vec{u}_i - \vec{\omega} \times \vec{r} \tag{1}$$

Based on the absolute velocity formulation, the governing equations of fluid flow (Navier-Stokes) within the framework of MRF can be written as follows:

$$\nabla \vec{u}_r = 0 \tag{2}$$

$$\nabla \left(\rho \vec{u}_r \vec{u}_i \right) + \rho \left[\vec{\omega} \times \vec{u}_i \right] = -\nabla p + \nabla \left(\bar{\bar{\tau}} \right) \tag{3}$$

where $\left[\vec{\omega} \times \vec{u}_i \right]$ represents the Coriolis and centripetal accelerations.

3.2.2 Reynolds Averaged Navier-Stokes Approach

In the stationary part of the computational domain, the basic Reynolds Averaged Navier-Stokes equations (RANS) [without Coriolis and centripetal acceleration (ω =0)] were applied. These equations are mainly based on the decomposition of Reynolds (Reynolds, 1894), where each instantaneous property (exact) *u* is decomposed into an average component (ensemble-averaged or time-averaged) *U* and fluctuating component *u'* (Schlichting, Gersten, Krause, Oertel, and Mayes, 1960; Wilcox, 1993).

In the momentum equations, the RANS equations form an additional term, called the Reynolds-stress tensor:

$$\tau_{ij} = \rho \overline{u_i' u_j'} \tag{4}$$

This leads to an increase in number of unknowns that is greater than that found in the equations. Additional equations are needed in order to close the problem. In this study, four turbulence models were applied in order to close the RANS equations.

3.2.3 Turbulence Models

For this study, four models were tested for resolution of the system. They were based on the Boussinesq hypothesis (Boussinesq, 1877; Schmitt, 2007) for relating the Reynolds stress tensor to the mean velocity gradients.

The Spalart-Allmaras model (Spalart and Allmaras, 1992) is among the simplest models based on a one-transport equation, in which the equation's variable is the kinematic eddy turbulent viscosity. This model was created especially for aerospace applications in compressible external flows over obstacles. This model has been shown to yield good results, especially in cases involving adverse pressure gradients. Among the advantages of this model is its ability to reduce computation time as compared to other models, and it easily provides stability and convergence for the solution.

The standard k-ε model (Launder and Spalding, 1972) is the first of two transport equation turbulence models. It is based on one equation for turbulence kinetic energy (k) and a second for its dissipation rate (ε). It is a semi-empirical model that is used widely in industrial problems due to its economical aspects and reasonable accuracy.

Several modifications have been proposed to optimize the weakness of the standard k-ε turbulence model. Among the most widespread extensions of the standard model is the k-ε (RNG) model proposed by (Yakhot and Orszag, 1986). This model is based on an introduction of the statistical technique known as the renormalization group theory. Swirl was among the major optimizations added to this model: this led to improved accuracy in turbulent swirling flows around complicated geometries, and uses an analytical formula to compute the Prandtl numbers; the standard k-ε model is based on constant values.

The standard k-ω model (Wilcox, 1993, 2008) is a low Reynolds model developed for treating the boundary layers close to the wall. This model is based on two transport equations: one for kinetic energy (k) and the other for the specific dissipation rate *(*ω) which is given by *(*ε). The standard Wilcox model is well known for its problems of convergence due to the sensitivity solution of the (k) equation outside the boundary layer.

Meanwhile, the k-ω SST model proposed by (Menter, 1994) was brought in to reduce this problem. The k-ω SST model is based on combining the standard k-ω formulation close to the wall with the standard k-ε model outside the boundary layers; this model has been shown to give good results, especially in stationary boundary layer applications.

The last model tested in this study is the transition SST model (Langtry and Menter, 2009) (also known as the γ-Re$_θ$ model). This model is an extension of the k-ω SST model; it is based on four transport equations: the first for kinetic energy (k); the second for the specific dissipation rate *(*ω); the third for intermittency (γ); and the fourth for the transition onset criteria of the momentum-thickness Reynolds number *(*Re$_θ$). The main advantage of this model is that it can treat laminar-turbulent transition flow phenomena.

3.3 Grid Generation

In each CFD simulation, it is crucial to begin by studying mesh independence, in order to find a type of mesh, where the results not be altered by the refinement of the mesh. An estimation of numerical error can be applied in order to evaluate the quality of numerical results. A number of methods exist for evaluating numerical error. One of the most popular methods is the Grid Convergence Index (GCI) method (Roache, 1994), which is based on the generalized extrapolation theory first proposed by Richardson (Celik and Karatekin, 1997; Richardson and Gaunt, 1927).

This method allows error to be estimated with regard to the mesh with no need for an analytical solution of the problem. For this purpose, error is estimated using a power function of characteristic mesh size. Several variants based on this method exist; in this project, the technique outlined by Celik *et al.* (Celik, Ghia, and Roache, 2008) was used. In order to evaluate numerical error using the GCI method, three types of mesh were needed, given the refinement grid factor that was greater than 1.3, a recommended value based on experimentation. In order to apply this method, the following basic steps were taken:

1. Define the representative mesh size, *h*:

$$h = \left[\frac{1}{N} \sum_{i=1}^{N} \Delta V_i \right]^{\frac{1}{3}} \tag{5}$$

where ΔV_i is the volume of the ith cell, and *N* is the total number of cells.

2. Find the overall variable chosen for each simulation, *φ* (torque, in this case) for different grids using the refinement factor:

$$r = \left[h_{coarse} / h_{fine} \right] > 1.3 \tag{6}$$

3. Calculate the apparent order (ξ) via the nonlinear relation:

$$\xi = \frac{1}{\ln(r_{21})} \times \left| \ln \left| \frac{\varepsilon_{32}}{\varepsilon_{21}} \right| + ln \left[\frac{r_{21}^\xi - s}{r_{32}^\xi - s} \right] \right| \tag{7}$$

Where $\quad s = sign(\varepsilon_{32} / \varepsilon_{21}) \quad ; \quad r_{21} = h_2 / h_1$

$\varepsilon_{21} = \varphi_2 - \varphi_1$ and $\varepsilon_{32} = \varphi_3 - \varphi_2$

4. Employ the grid convergence index (GCI) suggested by (Celik *et al.*, 2008) for the fine mesh solution, which can be expressed as:

$$GCI_{fine}^{21} = \frac{1.25 e_a^{21}}{r_{21}^P - 1} \tag{8}$$

Where $e_a^{21} = \left| (\varphi_1 - \varphi_2) / \varphi_1 \right|$ is the relative error.

The GCI value indicates how far the solution is from the asymptotic solution. In this study, the equation (7) was resolved numerically using the Newton iteration method. Table 3 shows the mesh cases chosen and detailed results on the case *(U$_{tunnel}$ = 10 (m/s))*, using the *k-ω SST* turbulence model for low Reynolds models and the *k-ε* (RNG) for high Reynolds models.

From the data illustrated in Table 3, we observe the numerical error between coarse and medium meshes for two cases (GCI^{32} ≈ 10.5% in low Reynolds models and GCI^{32} ≈ 2% for high Reynolds models) as well as the numerical error between fine and medium meshes in two other cases (GCI^{21} ≈ 3% for the low Reynolds case and GCI^{21} ≈ 1% for the high Reynolds case). This means that the discretization error is logically decreased by reducing the size; however, calculation time is increased. The values of GCI^{21} and ea^{21} have been accepted as reasonable errors for both cases.

Table 3 Estimation of discretization error using the Grid Convergence Index (GCI) method

	Case Mesh	Nodes Number	e_a (%)	Refinement factor, r	GCI (%)
Low Reynolds Mesh	1	15122510	0.56122	1.3690	2.9343
	2	5894230			
	3	2341683	1.94610	1.3603	10.541
High Reynolds Mesh	1	6836854	0.9928	1.3635	1.2535
	2	2697226			
	3	1171613	1.7129	1.3204	2.1785

Therefore, in this study, Mesh 2 in each case was chosen for all investigation tests. The mesh selected for low Reynolds models contained approximately 5.9 million tetrahedral mesh nodes in the one-third computational domain. The height of the first-floor mesh element was approximately 5×10^{-7}, ensuring that y+ would remain below 1 on the blade surface. The mesh selected for high Reynolds models contained approximately 2.7 million tetrahedral mesh nodes. The height of the first-floor mesh element was approximately 4×10^{-4}, which ensured that y+ was close to 30 on the blade surface when the logarithmic wall function was applied in the fully turbulent region.

3.4 Boundary Conditions

In this study, the boundary conditions used are as follows:

A constant uniform velocity corresponding to each case of the new MEXICO experiments (Table 2) was specified in the inlet of the computational domain. Turbulence intensity was defined as a low value, I=0.2 %, as it had been in the experiments done by (Boorsma and Schepers, 2014).

In the outlet boundary, static pressure was imposed and was equal to the ambient pressure of the wind tunnel corresponding to each case (Table 2).

The MRF was applied to the rotating part of the domain with a constant rotational speed of 425.5 (rpm).

An interface technique was applied to separate rotating parts from stationary parts. Because the velocities in both the rotating and stationary parts were stored in the absolute frame, velocities were determined in the interface between two domains based on absolute velocity; scalar quantities such as density and pressure were calculated locally, from adjacent cells.

4. RESULTS AND DISCUSSION

4.1 Pressure Coefficient

Distribution of measured and calculated local surface pressure coefficients surrounding the five spanwise sections of the blade were compared, as shown in Figs. 5, 6, and 7. For the first case investigated (Fig.5), U_{tunnel} =10 (m/s) was categorized as having low wind speed. Flow was mostly attached and pressure distribution for all the turbulence models showed very good agreement, with the exception of the inboard sections at low wind speed, where we know from (Boorsma and Schepers, 2014; Sørensen *et al*., 2016) that the pressure sensors' range is insufficient for resolving the actual physics. This reflects the ability of both low and high Reynolds RANS turbulence models to predict attached flows.

In the second case investigated, however, U_{tunnel} =15 (m/s), which has been categorized as the onset of stall (Fig. 6). Good agreement with experimental data was seen for the high Reynolds models. Good agreement was also observed for the transitional γ-Re_θ low Reynolds model. For the k-ω SST low Reynolds model, good agreement in the region below 60% was observed in the blade span. This said, marked deviation was seen in the outer part of the blade, in the NACA region. This was due to a weakness of the k-ω SST model in solving flow in the separate zones, and to the ability of the γ-Re_θ model to resolve the transition laminar with regard to turbulent boundary layers.

Figure 7 shows the pressure coefficient distributions in the last case investigated, U_{tunnel} =24 (m/s); these were classified as separated flow conditions. Good agreement was observed in the DU airfoil region, in the near-root part of the blade for low Reynolds models. Starting from 60% of the blade's span, there was a deviation in the extrados, especially in the area close to the leading edge. This explains the difficulty on the part of both k-ω SST and γ-Reθ low Reynolds models in solving full separated flows.

Otherwise, good agreement was obtained by both the k-ε (RNG) and the Spalart-Allmaras high Reynolds models, reflecting the effect of the wall functions in full separated flows. Very good agreement, especially for the k-ε (RNG) model, was observed, due to this model's ability to solve the separate turbulent boundary layers in high Reynolds numbers.

Figure 8 shows the streamlines in the suction side of the blade, simulated in three cases (U_{tunnel} =10, 15 and 24 (m/s)) using the k-ε (RNG) turbulence model. At U_{tunnel} =10 (m/s), we see that flow is attached to the whole blade at this low wind velocity; however, a slight radial component appearing at the root of the blade is noticeable, likely due to vortex shedding in this region.
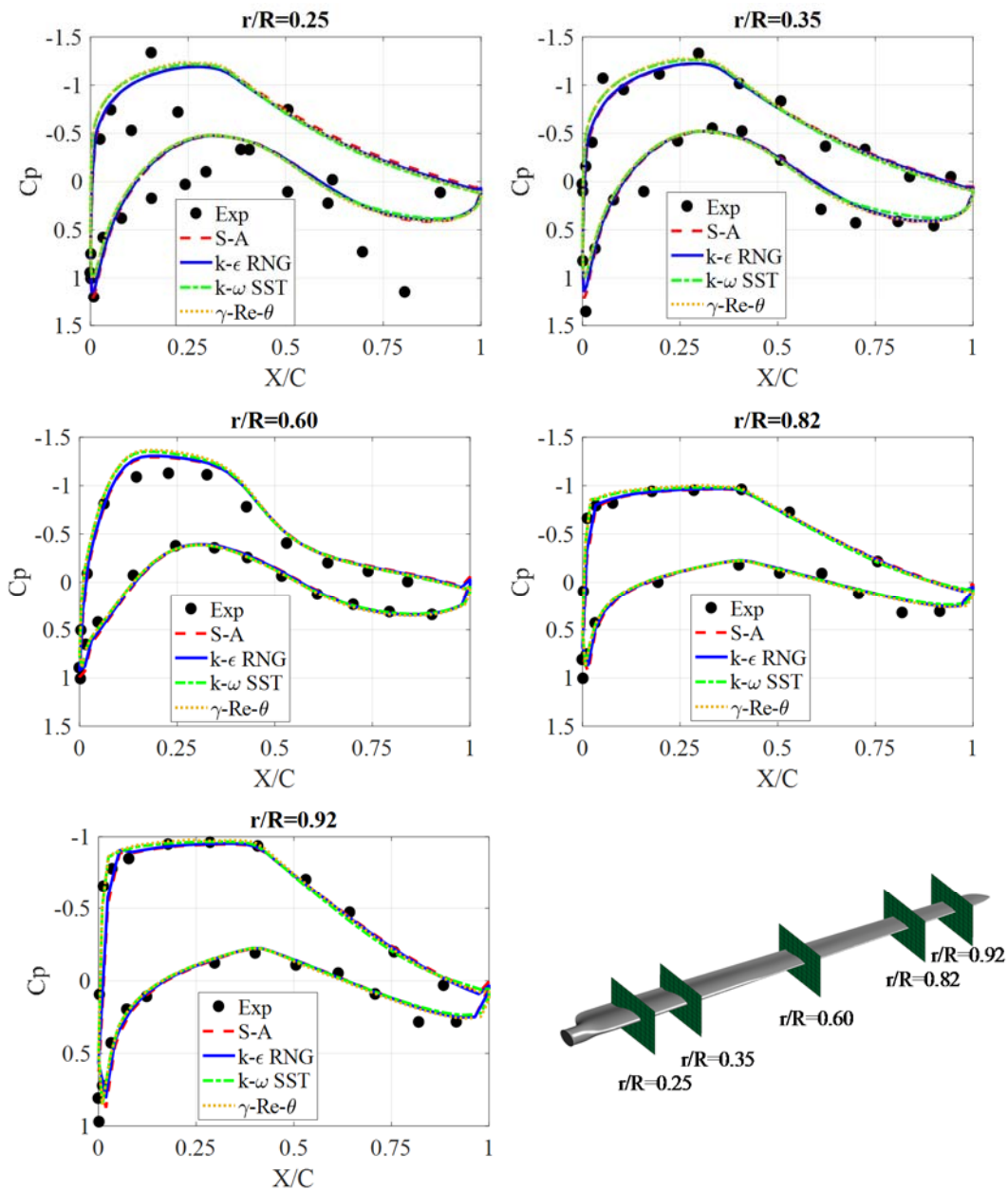
Fig. 5. Pressure coefficient distributions at five spanwise sections for case 1 (U$_{tunnel}$ =10 (m/s)), comparing experimental values with CFD results.

In the second case, where *U$_{tunnel}$ =15 (m/s)*, this separated component increased somewhat in the root part of the blade, especially along its leading edge; the flow remained attached in the blade.

At a wind speed of *24 (m/s)*, separations of flow appeared on the suction side of the entire blade, from its leading to its trailing edges, unlike what we observed in the first and second cases, where the separation zones did not exceed the 0.25 x R blade span. The separation zone rose higher than the 0.92 x R region in the third case, reflecting an increased wind speed effect on boundary layer separation.

4.2 Blade Loads

CFD computations of low and high Reynolds models

were compared to the measured data, with respect to integral loads. The loads, in both the experiment and in computations, were derived from the five sectional pressure distributions by integration. Integration was based on a simple linear variation between the sections assuming zero value at the root and tip of the blade. Because viscous friction contributions are not available in the experiment, friction is not included in the load determination from the CFD computations (Boorsma and Schepers, 2014; Sørensen *et al*., 2016).

Figure 9 shows the normal and tangential force distribution in the three cases studied.

In the first case, where the flow was mostly attached, good agreement with experimental data was
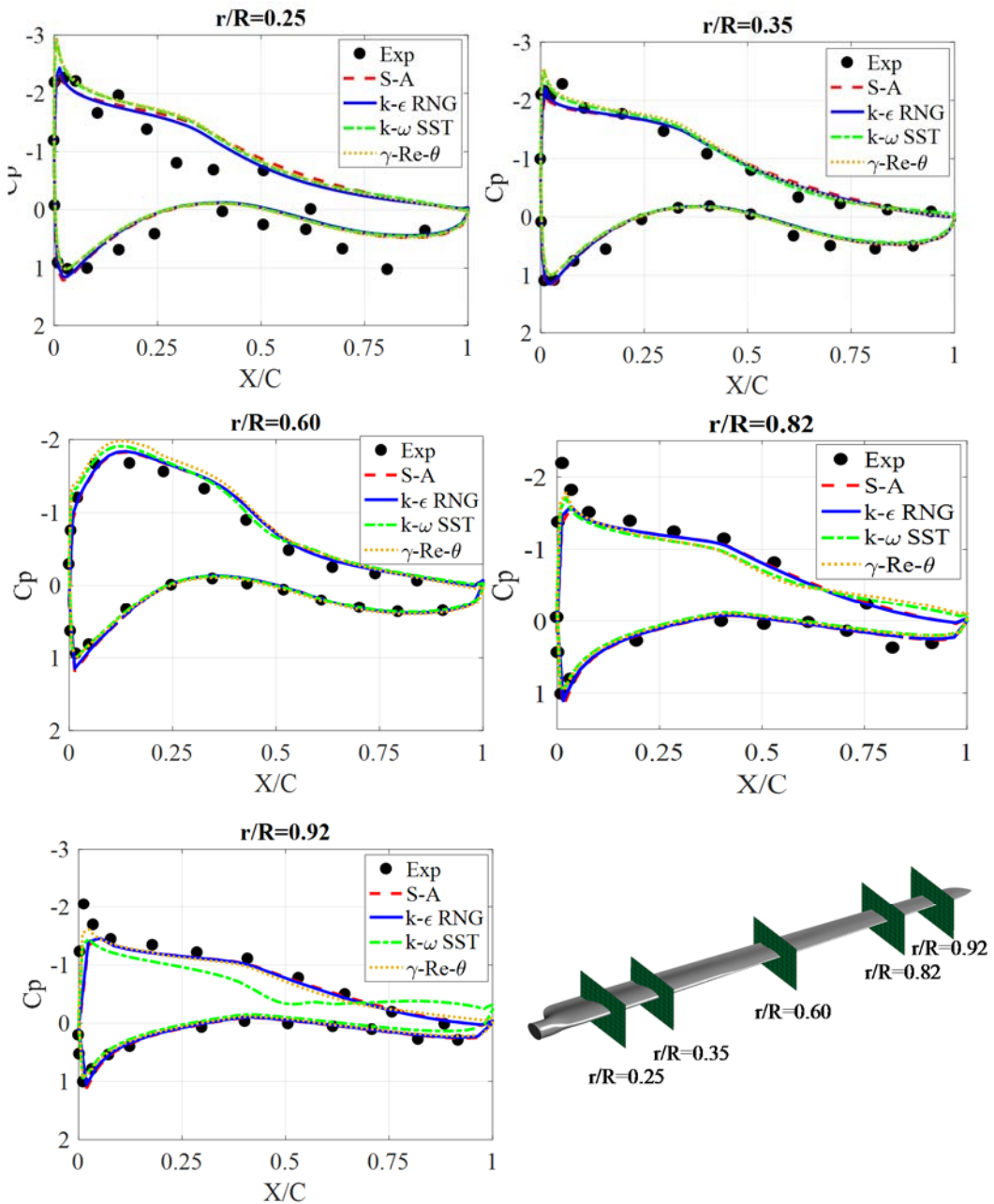
158

Fig. 6. Pressure coefficient distributions at five spanwise sections for case 2 ($U_{tunnel} = 15$ (m/s)), comparing the experimental values with CFD results.

observed for all types of turbulence models. In this region, the best model was the transition γ-Re$_\theta$ model. In the second case, at the onset of stall, where $U_{tunnel} = 15$ (m/s), deviation was detected in the outer part of the blade: the low Reynolds models showed the greatest amount of deviation in this region, due to the difficulty low Reynolds models have in resolving separation flow. The same results were found for case 3, $U_{tunnel} = 24$ (m/s), although in this case, even the Spalart-Allmaras high Reynolds model was divided. The model most able to capture the forces was the k-ε (RNG) model. The inability of the Spalart-Allmaras model to solve separated flow and the ability of the k-ε (RNG) model to predict

separated flow resulted in both models being adopted in order to resolve wall corrections; this was probably due to the effect of swirl modeling on turbulence included in the k-ε (RNG) model.

4.3 Velocity In The Near Wake

In order to examine the effect of the selected turbulence models on mean velocity in the wake, axial velocity profiles along a line at $r = 1.5$ (m), at the 9 o'clock position plan were compared for three cases, with blade 1 pointing vertically up ($U_{tunnel} = 10, 15$ and 24 (m/s)) (Fig. 10). In the first case, similar results were obtained for all turbulence models, accompanied by very good agreement with experimental data. In the second case, there was
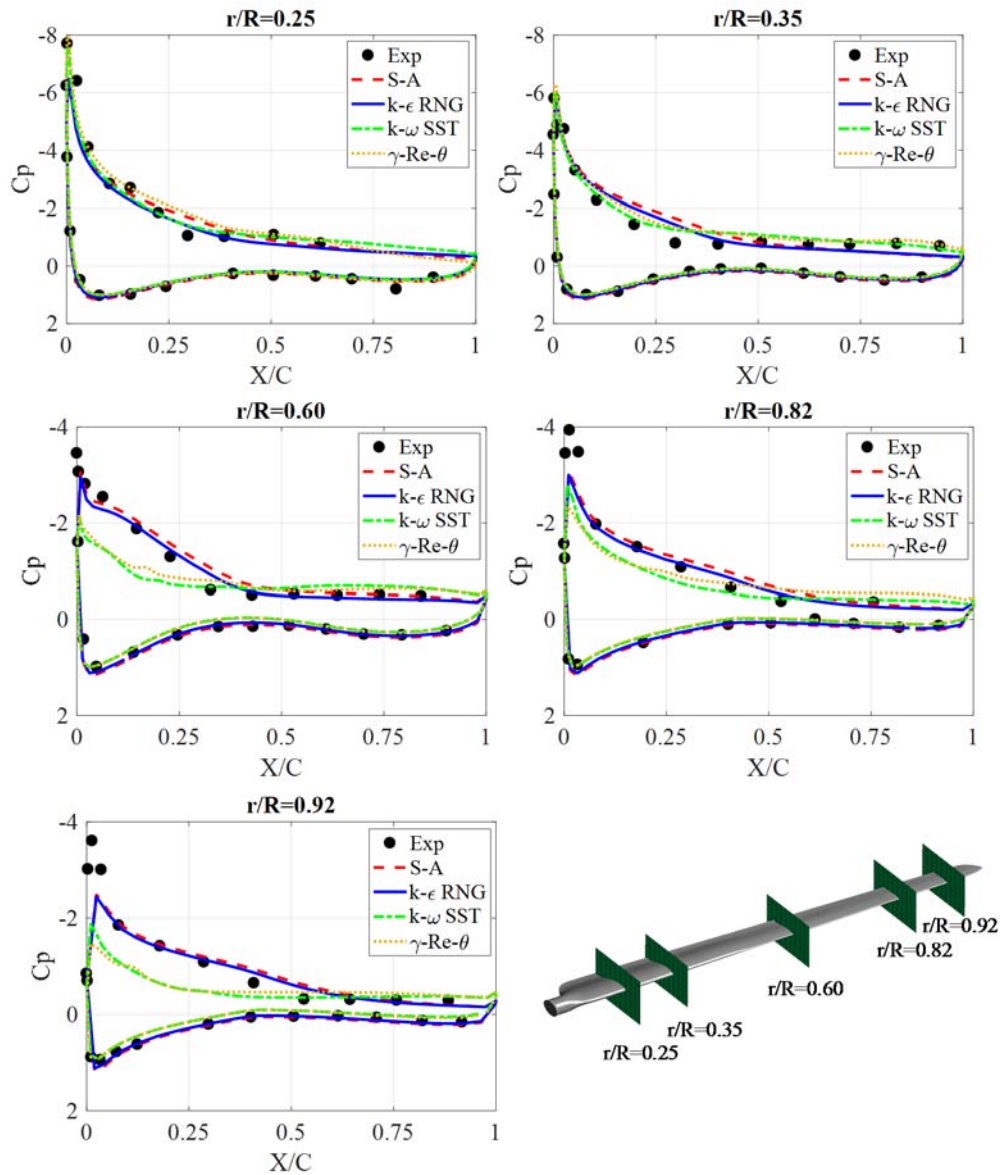
Fig. 7. Pressure coefficient distributions at five spanwise sections for case 3 (U_{tunnel} =24 (m/s)), comparing the experimental values with CFD results.
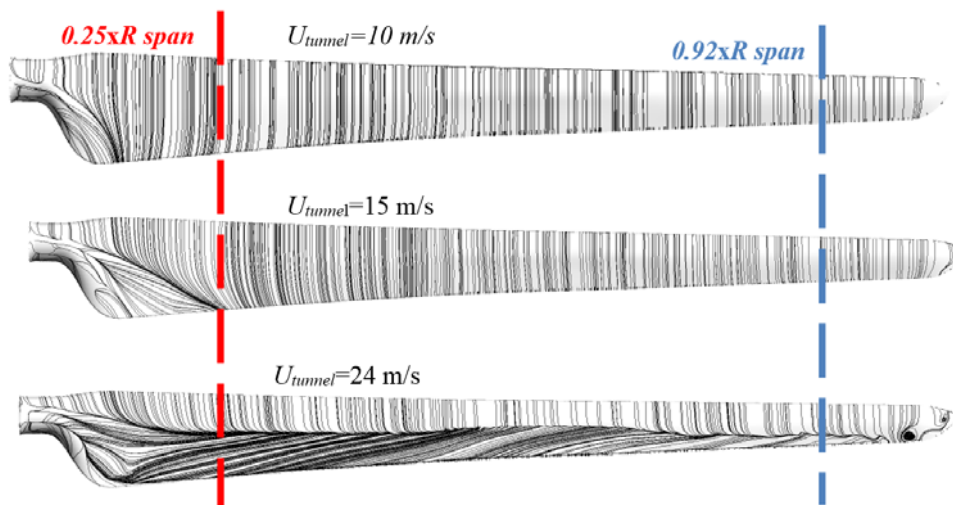

Fig.8. Limiting streamlines on the suction side of the MEXICO blade for three cases for high Reynolds models.
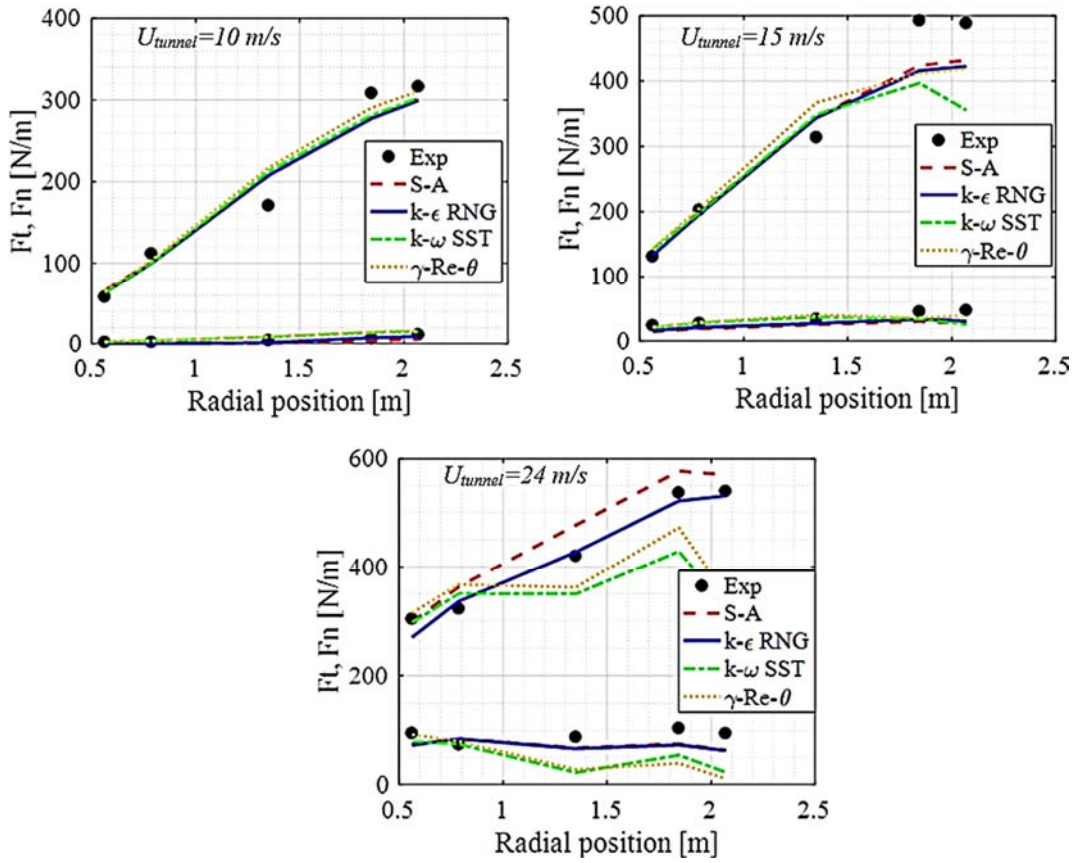
Fig. 9. Normal and tangential force distribution for three cases (U_{tunnel} = 10, 15 and 24 (m/s)).
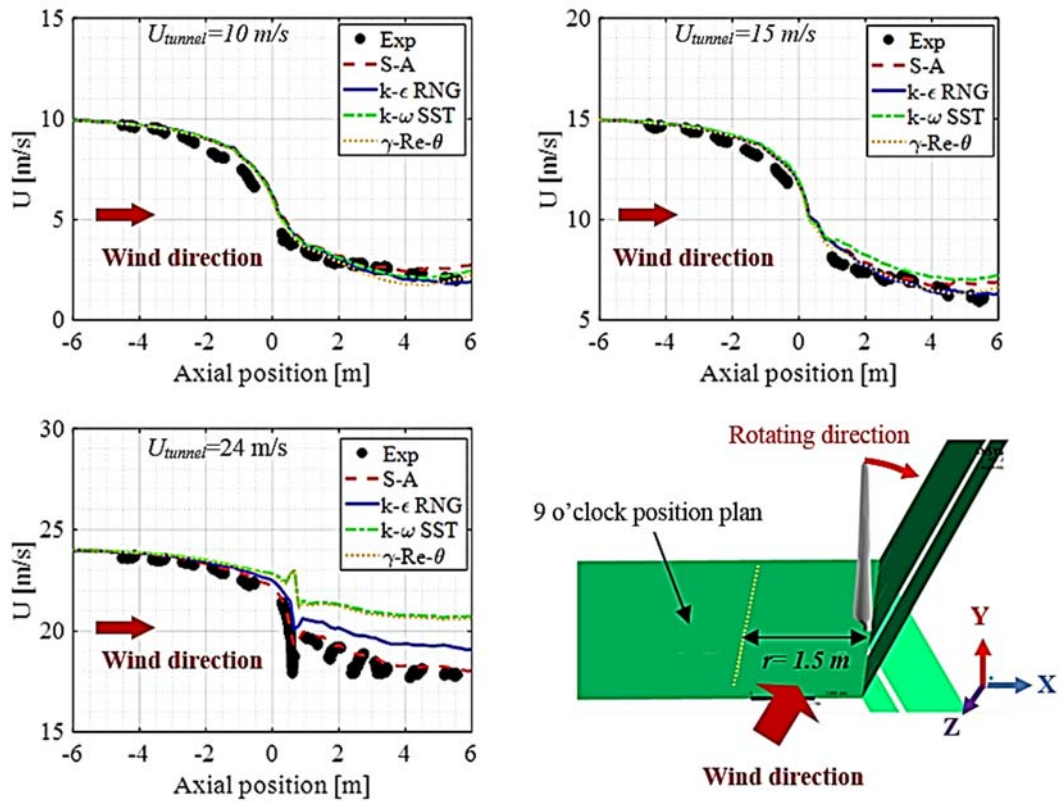

Fig. 10. Axial velocity profiles along a line at r=1.5 (m), at 9 o'clock position, with blade 1 pointing vertically up, for three cases (U_{tunnel} = 10, 15 and 24 (m/s)).
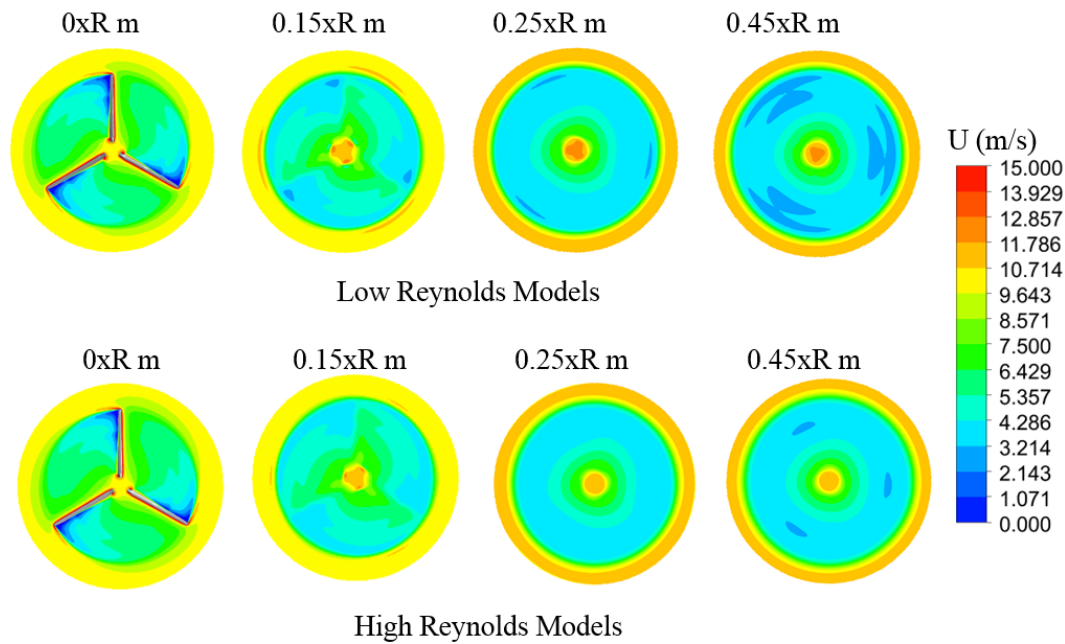
0xR m   0.15xR m   0.25xR m   0.45xR m

Low Reynolds Models

0xR m   0.15xR m   0.25xR m   0.45xR m

High Reynolds Models

Fig. 11. Velocity contours behind the blade, comparison of low and high Reynolds models ($U_{tunnel} = 10$ (m/s)).

0xR m   0.15xR m   0.25xR m   0.45xR m
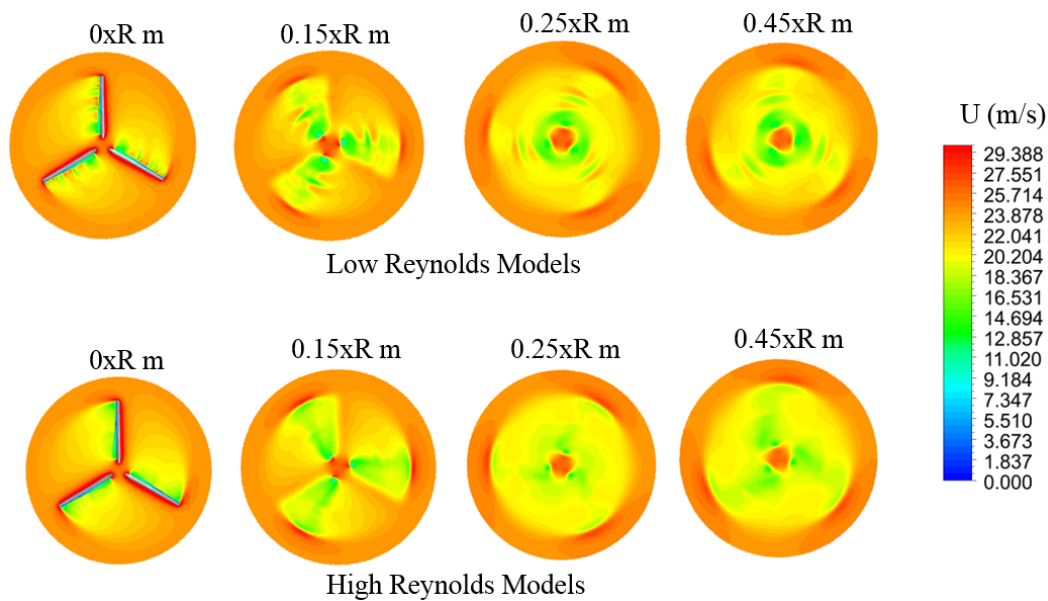
Low Reynolds Models

0xR m   0.15xR m   0.25xR m   0.45xR m

High Reynolds Models

Fig. 12. Velocity contours behind the blade, comparison of low and high Reynolds models ($U_{tunnel} = 24$ (m/s)).

good agreement for all models except the SST model in downstream flow, which saw a slight deviation due to the difficulty of swirl modeling; this was probably due to difficulty in resolving boundary layers. In the last case, where flow was separated, deviation was noted in the downstream for all turbulence models save the Spalart-Allmaras model, which yielded good agreement.

Figure 11 shows the mean axial downstream velocity contours behind the rotor for both high and low Reynolds models, for a wind speed of *10 m/s*. The results show that the velocity intensity between the two formulations was almost the same in this case, where flow was mostly attached. However, in the case of high wind speed ($U_{tunnel} = 24$ (m/s)), (Fig. 12), we see that the mean velocity intensity for the low Reynolds models was higher than for the high Reynolds models, and that explains the over-prediction of downstream velocity which was noticed in Fig. 10. It was therefore concluded that modeling along the near wall influenced the distribution of velocity behind the rotor, and correction of the wall can reduce the over-prediction of velocity.

5. CONCLUSION

The effects of four RANS turbulence models in two near-wall treatment approaches (high and low Reynolds models) on predicting the aerodynamic performance of a horizontal axis wind turbine rotor were studied numerically over a range of wind conditions, where flow over the rotor changed from fully attached flow to massively separated flow. The new MEXICO experiments recently carried out at the large-scale, low-speed facility (LLF) of the German Dutch wind tunnels (DNW) were used to validate the numerical simulation. Because the experiments were carried out in the open-jet section of this high-quality wind tunnel, the effect of the tunnel was not taken into account, as shown in the reference (Shen *et al.*, 2012). The results can be generalized for real atmospheric conditions.

As results of this study, it was found that:

o All the studied turbulence models did a reasonable job of predicting aerodynamic performance and velocity in the wake, at low wind speeds.

o With an increase in wind speed, differences between models became apparent.

o Transition modeling in low Reynolds models had a marked effect only at low wind speeds.

o Modeling of the near wall was shown to play a sensitive role in predicting blade loads and velocity in the near wake.

o Generally, for high wind speeds, it was found that the high Reynolds models yielded good results as compared with the low Reynolds models.

o Modeling of the swirl effect with wall corrections in both transport equations for the k-ε model was considered to be the best model, yielding the best accuracy within a reasonable computational time.

ACKNOWLEDGEMENTS

REFERENCES

Abdulqadir, S. A., H. Iacovides and A. Nasser (2016). The physical modelling and aerodynamics of turbulent flows around horizontal axis wind turbines. *Energy*.

ANSYS Fluent. (2016). 16.2 Fluent Theory Guide Documentation.

Aranake, A. C., V. K. Lakshminarayan and K. Duraisamy (2015). Computational analysis of shrouded wind turbine configurations using a 3-dimensional RANS solver. *Renewable Energy 75*, 818-832.

Boorsma, K. and J. Schepers (2014). *New Mexico Experiment, Preliminary overview with initial validation*. Technical report.

Bouhelal, A., A. Smaili, C. Masson and O. Guerri (2017). Effects of Surface Roughness on Aerodynamic Performance of Horizontal Axis Wind Turbines. *The 25th Annual Conference of the Computational Fluid Dynamics Society of Canada, CFD2017-337, University of Windsor*.

Boussinesq, J. (1877). *Essai sur la théorie des eaux courantes*: Imprimerie nationale.

Celik, I. B., U. Ghia and P. J. Roache (2008). Procedure for estimation and reporting of uncertainty due to discretization in CFD applications. *Journal of Fluids Engineering 130*(7).

Celik, I. B. and O. Karatekin (1997). Numerical experiments on application of Richardson extrapolation with nonuniform grids. *Journal of Fluids Engineering (588), 119*.

Elfarra, M. A., N. Sezer Uzol and I. S. Akmandor (2014). NREL VI rotor blade: numerical investigation and winglet design and optimization using CFD. *Wind Energy 17*(4), 605-626.

Fingersh, L., D. Simms, M. Hand, D. Jager, J. Cotrell, M. Robinson and S. Larwood (2001). *Wind tunnel testing of NREL's unsteady aerodynamics experiment*. Paper presented at the 20th 2001 ASME Wind Energy Symposium.

Guntur, S. and N. N. Sørensen (2013). *A Detailed Study of the Rotational Augmentation and Dynamic Stall Phenomena for Wind Turbines*. Technical report.

International Energy Agency, I. E. A. (2012). World energy outlook , doi:10.1787/weo-2012.

Langtry, R. B. and F. R. Menter (2009). Correlation-based transition modeling for unstructured parallelized computational fluid dynamics codes. *AIAA journal 47*(12), 2894-2906.

Launder, B. E. and D. B. Spalding (1972). Lectures in mathematical models of turbulence.

Luo, J. and A. Gosman (1994). *Prediction of impeller-induced flow in mixing vessels using multiple frames of reference*.

Menter, F. R. (1994). Two-equation eddy-viscosity turbulence models for engineering applications. *AIAA journal 32*(8), 1598-1605.

Moshfeghi, M., Y. J. Song and Y. H. Xie (2012). Effects of near-wall grid spacing on SST-K-ω model using NREL Phase VI horizontal axis wind turbine. *Journal of Wind Engineering and Industrial Aerodynamics 107*, 94-105.

Oggiano, L., K. Boorsma, G. Schepers and M. Kloosterman (2016). *Comparison of simulations on the NewMexico rotor operating in pitch fault conditions.* Paper presented at the Journal of Physics: Conference Series.

Plaza, B., R. Bardera and S. Visiedo (2015). Comparison of BEM and CFD results for MEXICO rotor aerodynamics. *Journal of Wind Engineering and Industrial Aerodynamics 145*, 115-122.

Reynolds, O. (1894). On the dynamical theory of incompressible viscous fluids and the determination of the criterion. *Proceedings of the Royal Society of London 56*(336-339), 40-45.

Richardson, L. F. and J. A. Gaunt (1927). The deferred approach to the limit. Part I. Single lattice. Part II. Interpenetrating lattices. *Philosophical Transactions of the Royal Society of London. Series A, containing papers of a mathematical or physical character 226*, 299-361.

Roache, P. J. (1994). Perspective: a method for uniform reporting of grid refinement studies. *Transactions-American Society of Mechanical Engineers Journal of Fluids Engineering 116*, 405-405.

Schepers, J., K. Boorsma, T. Cho, S. Gomez Iradi, , P. Schaffarczyk, A. Jeromin, B. Stoevesandt (2012). *Final report of IEA Task 29, Mexnext (Phase 1): Analysis of Mexico wind tunnel measurements*. Technical report

Schepers, J., K. Boorsma, S. Gomez Iradi, P. Schaffarczyk, H. A. Madsen, N. N. Sørensen and S. Schreck (2014). Final report of IEA Wind Task 29: Mexnext (Phase 2).

Schlichting, H., K. Gersten, E. Krause, H. Oertel, and K. Mayes (1960). *Boundary-layer theory* 7.

Schmitt, F. G. (2007). About Boussinesq's turbulent viscosity hypothesis: historical remarks and a direct evaluation of its validity. *Comptes Rendus Mécanique 335*(9-10), 617-627.

Schreck, S. (2002). The NREL full-scale wind tunnel experiment Introduction to the special issue. *Wind Energy 5*(2-3), 77-84.

Shen, W. Z., W. J. Zhu and J. N. Sørensen (2012). Actuator line/Navier–Stokes computations for the MEXICO rotor: comparison with detailed measurements. *Wind Energy 15*(5), 811-825.

Shepers, J. G. (2012). Engineering models in wind energy aerodynamics: Development, implementation and analysis using dedicated aerodynamic measurements, Phd thesis.

Simms, D., S. Schreck, M. Hand and L. Fingersh (2001). NREL unsteady aerodynamics experiment in the NASA-Ames wind tunnel: a comparison of predictions to measurements. *National Renewable Energy Laboratory, Golden, CO, Report No. NREL/TP-500-29494.*

Snel, H., G. Schepers and N. Siccama (2009). *Mexico Project: the database and results of data processing and interpretation.* Paper presented at the 47th AIAA Aerospace Sciences Meeting Including the New Horizons Forum and Aerospace Exposition.

Snel, H., J. Schepers and B. Montgomerie (2007). *The MEXICO project (Model Experiments in Controlled Conditions): The database and first results of data processing and interpretation.* Paper presented at the Journal of Physics: Conference Series.

Sorensen, N., J. Michelsen and S. Schreck (2002). *Navier-Stokes predictions of the NREL phase VI rotor in the NASA Ames 80-by-120 wind tunnel.* Paper presented at the ASME 2002 Wind Energy Symposium.

Sørensen, N. N., F. Zahle, K. Boorsma and G. Schepers, (2016). *CFD computations of the second round of MEXICO rotor measurements.* Paper presented at the Journal of Physics: Conference Series.

Spalart, P. and S. Allmaras (1992). *A one-equation turbulence model for aerodynamic flows.* Paper presented at the 30th aerospace sciences meeting and exhibit.

Thumthae, C. and T. Chitsomboon (2009). Optimal angle of attack for untwisted blade wind turbine. *Renewable Energy 34*(5), 1279-1284.

Wilcox, D. C. (1993). Turbulence modeling for CFD, DCW Industries. *Inc., California*.

Wilcox, D. C. (2008). Formulation of the kw turbulence model revisited. *AIAA journal 46*(11), 2823-2838.

Yakhot, V. and S. A. Orszag (1986). Renormalization group analysis of turbulence. I. Basic theory. *Journal of scientific computing 1*(1), 3-51.